TU Delft

Delft University of Technology

Ultraviolet Sensing in WBG SiC

Mansouri, Brahim el; Driel, W.D. van; Zhang, GuoQi

DOI
10.1007/978-3-030-16577-2_14

Publication date
2020

Document Version
Final published version

Published in
Sensor Systems Simulations

Citation (APA)
Mansouri, B. E., Driel, W. D. V., & Zhang, G. (2020). Ultraviolet Sensing in WBG: SiC. In W. van Driel, O. Pyper, & C. Schumann (Eds.), *Sensor Systems Simulations* (pp. 397-425). SpringerOpen. https://doi.org/10.1007/978-3-030-16577-2_14

Important note
To cite this publication, please use the final published version (if applicable).
Please check the document version above.

Copyright
Other than for strictly personal use, it is not permitted to download, forward or distribute the text or part of it, without the consent of the author(s) and/or copyright holder(s), unless the work is under an open content license such as Creative Commons.

Takedown policy
Please contact us and provide details if you believe this document breaches copyrights.
We will remove access to the work immediately and investigate your claim.

This work is downloaded from Delft University of Technology.
For technical reasons the number of authors shown on this cover page is limited to a maximum of 10.

Green Open Access added to TU Delft Institutional Repository

'You share, we take care!' - Taverne project

https://www.openaccess.nl/en/you-share-we-take-care

Otherwise as indicated in the copyright section: the publisher is the copyright holder of this work and the author uses the Dutch legislation to make this work public.

Chapter 14
Ultraviolet Sensing in WBG: SiC

B. El Mansouri, W. D. van Driel, and G. Q. Zhang

14.1 Introduction

The main application for the ultraviolet (UV) sensor is the detection of partial discharge associated with power grid equipment, but not limited to this. The UV electromagnetic radiation occupies the spectral range of 10–400 nm. The UV radiation is used in many applications ranging from chemical processes such as lithography to biology. The UV spectral range is typically divided into four wavelength (λ) regions as illustrated in Fig. 14.1.

The photodetection is then also classified according to the UV range of interest [1–4]. The photodetectors are referred to as solar-visible for the spectral range above UVA [1]. Another special range is the deep UV (DUV) range of 220–280 nm [1, 3]. Here the DUV radiation from the sun is mostly absorbed by the ozone layer leaving longer wavelengths than 280 nm (UVC) to reach earth. This gives the opportunity to use photodetection in the lower wavelength region without being affected by the sun, hence the classification as solar blind photodetection. As for wavelengths shorter than 200 nm, these will be absorbed by the oxygen in the atmosphere. The photodiodes can further be classified depending on the used materials, structure of the sensor, insulation, filtering and so on.

Most common photodetectors are semiconductor based, i.e. photoconductors, photodiodes such as PN, pin and MS and MSM diodes, and phototransistors.

B. El Mansouri · G. Q. Zhang
Delft University of Technology, EEMCS Faculty, Delft, The Netherlands
e-mail: B.ElMansouri@tudelft.nl; G.Q.Zhang@tudelft.nl

W. D. van Driel (✉)
Delft University of Technology, EEMCS Faculty, Delft, The Netherlands

Signify, HTC48, Eindhoven, The Netherlands
e-mail: willem.van.driel@signify.com; willem.van.driel@philips.com

© Springer Nature Switzerland AG 2020

W. D. van Driel et al. (eds.), *Sensor Systems Simulations*,
https://doi.org/10.1007/978-3-030-16577-2_14

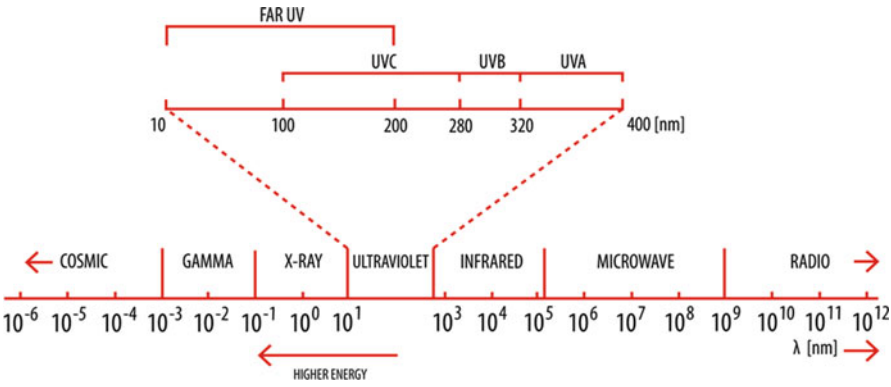

Fig. 14.1 The electromagnetic spectrum with the highlighted UV range

Semiconductor devices are attractive thanks to their small size, lightweight and insensitivity to magnetic fields. Moreover, they can have good sensitivity, linearity and high-speed operation [5]. The devices, each have strengths and weaknesses enabling the detection of various optical signals in different fields ranging from simple applications such as sunshine detection, to industrial or military applications such as corona discharge, flame detection or missile plume detection.

The aim here is to use SiC as a starting material. SiC is a WBG semiconductor and has the advantage of high responsivity, high thermal stability, robust radiation hardness, high response speed and high power [1]. Next to this, the photodetector should be sensitive to low light level in the range of fW–aW/cm^2 while having a clear distinction from the noise level and maintaining a reliable signal.

The photodetectors can be selected based on the detection signal. Each optical source may emit photons at a different spectral range and have a certain signal strength. This translates in various requirements which also motivates the device type selection. The requirements may include:

- Spectral range of the optical signal.
- The optical signal strength.
- Linearity of the output signal.
- Response time (speed).

Each of these requirements has additional restraints on the selection of the device. Take for example the minimum detectable signal which sets the noise floor and dark current requirements. Or the upper limit of the signal detection which is determined by the maximum current that the detector can handle without becoming saturated. All these restraints are then translated in the minimum sensitivity or responsivity, the detectivity and NEP requirements.

14.1.1 Applications

UV photodetection has potential for many applications in both civil and military fields which may include flame detection, missile threat detection, water treatment, astronomical observations, telecommunications, environmental monitoring and many more. One of the most interesting applications is the corona discharge at the electrical power networks. This is key because it manages the energy needs of societies in the form of electricity. It is then important for critical applications such as missile threat or flame detection, requiring good temperature stability of the photodetectors, to have a reduction in errors for a reliable signal [1, 2, 5–7]. In space applications, for optical communications such as inter-satellite communications, $\lambda < 280$ nm can be useful and for the industry related applications such as instrumentation and UV lithography emitter calibration can be used [5]. Next to the application, the device type is selected based on the signal type, signal strength for detectability, environmental conditions and so on. Table 14.1 lists some examples of the applications.

14.1.2 State of the Art

The UV detection in the state grid is currently applied using UV cameras such as "UV-260 Corona Discharge Camera" and "DayCor Superb UV imager" which superimposes the detected UV light on a normal image to show the location [8]. The "DayCor Superb UV imager" has a UV sensitivity of 2.2×10^{-18}W/cm^2 and a minimum visible light detection of 0.1Lux. The minimum discharge detection is 1 pC at a distance of 10 m. The spectral range is kept within 240–280 nm as this corresponds to the solar blind range allowing for daytime detection. The discharge severity can then be estimated based on the photon number [8]. However, this method is only used at close range while needing someone to operate it. This

Table 14.1 Examples for UV detection applications

Applications	Harsh environment
UV lithography (193 nm)	–
UV curing processing (365 nm)	–
Disinfection of water and air (240–290 nm)	–
Detection of corona discharges (<280 nm)	YES
Early missile (plume) threat detection	YES
Chemical and biological threat detection	–
Flame detection/combustion monitoring	YES
Environmental monitoring (ozone/pollutants)	YES
Optical communications, e.g. space (<280 nm)	YES
Astronomical studies	–

shows that developing sensors that can be employed over the entire grid offer better monitoring of the power grid.

Next to the camera, an imaging system was also developed to detect ultraviolet detection [9, 10]. The imaging sensor is able not only to detect hydrogen flames but also corona discharge at a proximity. The UV light intensity detected for the latter is 37 nW/cm^2 with a 400 lux background light intensity. The imaging sensor is based on CMOS technology while the photodetection is obtained using an organic photoconductive film (OPF). The film is not only sensitive in the UV range but also in the visible range and therefore a smart imaging scheme was used to detect both the visible and UV radiation at the same time. This enables a normal image with an imposed UV image.

14.2 Device Types

There are various technologies used for photodetection application ranging from vacuum tube devices used as photomultipliers (PMTs) to semiconductor devices such as photoconductor, Schottky diodes and pn-junctions including their adaptations [1, 5]. Here, two structure types are used, the MSM and device types. Therefore, the discussion in this chapter will limit itself to the discussion and development of these devices.

14.2.1 The Photoconductor

The photoconductor, also referred to as a photoresistor, is an ohmic photodetector. The device has a simple design comprised of a pair of ohmic electrodes with on the top surface a highly doped semiconductor absorbing layer and an electrode on each side, as shown in Fig. 14.2.

The MSM photoconductor allows for simple fabrication not only reducing cost but is an advantage as no additional epitaxial layer is needed and hard materials such as SiC are less of an issue regarding implantation, diffusion and etching. Further the device can realize a large area of detection. The conductivity of the semiconductor

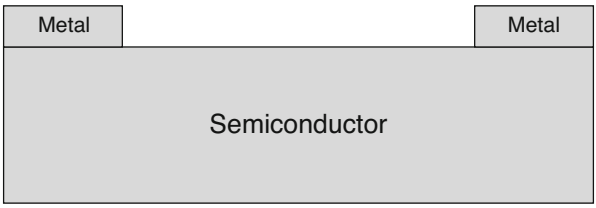

Fig. 14.2 Metal-semiconductor-metal photoconductor

is dependent on the amount of incident photons which in turn excite electrons to the conduction band enabling a higher conductivity of the material. When the electrodes are biased, the electrical field will drive the photogenerated e-h pairs to separate and move towards the electrodes resulting in a photocurrent in the external circuit proportional to the photon lux [1]. In the absence of incident photons, the dark current of the device is given by

$$I_{\mathrm{d}} = \frac{V}{R_{\mathrm{d}}} \tag{14.1}$$

where R_{d} is the resistance of the material in the dark. Since the conductivity is dependent on the incident photons with sufficient energy, the resistance of the semiconductor will drop resulting in a photocurrent given by

$$I_{\mathrm{p}} = V\left(\frac{1}{R_{\mathrm{i}}} - \frac{1}{R_{\mathrm{d}}}\right) \tag{14.2}$$

where R_{i} is the resistance under illumination. Figure 14.3 illustrates the *I-V* characteristics of the photoconductor in the dark and under illumination [2].

The full expression for the photocurrent in a photoconductive device is given by [11]

$$I_{\mathrm{p}} = \left(\frac{P_{\mathrm{opt}}}{h\upsilon}\right) q\eta G = \left(\frac{P_{\mathrm{opt}}}{hc}\right) \lambda q \eta G \tag{14.3}$$

with

$$G = \frac{\mu \tau V}{s^2} \tag{14.4}$$

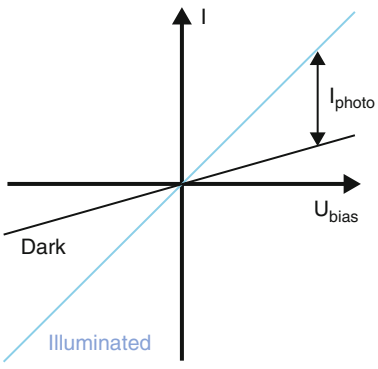

Fig. 14.3 *I-V* characteristics of a photoconductor

where P_{opt} is the incident optical power, V is the applied voltage, q is the electron charge, η is the quantum efficiency (QE), hv is the photon energy, λ is the wavelength, c is the speed of light, G is the photoconductive gain, μ is the electron mobility, τ is the carrier lifetime and s is the inter-electrodes spacing.

The performance of the photoconductor depends on a number of physical parameters. For instance, a trade-off between a high gain G and a fast response has to be found for longer recombination lifetime of the holes making the device slower. The photoconductive nature of the device is that it requires a bias which inherently adds dark current to the noise contributions which reduces the minimum detectable optical signal. Moreover, the electric field effects such as space charge limited current, avalanche and dielectric breakdown limit the photocurrent and therefore become an issue for scaling down of photoconductor devices for higher end applications. The scaling down is further limited by the area required for optical sensing to obtain any useful optical signal especially for devices with metallic electrodes which reflect light. This drawback can be reduced through transparent electrodes such as Indium Tin Oxide (ITO) or 2D materials such as graphene which is the case for this work. The device can further be enhanced by using nanomaterials on the top surface which results in a high photo conductive gain G and high responsivity [12].

Some of the drawbacks such as large area requirement render the device only useful for applications with slower speeds. Further the output signal of the device will also depend on previously detected signals due to a photo memory effect. The photoconductive nature of the device also gives rise to a nonlinear relation between the resistance and illumination E_i as given by equation

$$R = AE_i^{-\alpha} \tag{14.5}$$

where A and α are constants depending on the semiconducting material and the processing used to manufacture the device. Since the device changes resistance, it is also highly temperature dependent adding to uncertainty of the optical signal in the form of thermal noise.

14.2.2 MSM Schottky Photodetector

In the previous section, the MSM structure was shown to be applicable as a photoconductive device. The same structure can be utilized for Schottky type photodetectors by using intrinsic or low doped semiconductors with an appropriate metal to create a high enough Schottky barrier [13]. The contacts can be made as interdigitated electrode fingers (IDT) which result in back-to-back diodes and by combining this with semiconductors having a wide bandgap, UV photodetection is enabled [2, 13, 14]. The biasing of the two diodes will always result in reverse operation of one diode while the other is in forward bias enabling the conduction of the current. As was discussed in the previous text for the photoconductor, the device

is simple to fabricate, but has additional advantages such as low dark current, low junction capacitance, high bandwidth (BW) and is CMOS compatible [13, 15, 16].

To analyse the behaviour of the MSM, first consider the metal-semiconductor (MS) Schottky diode shown in Fig. 14.4.

As was mentioned in earlier text, when a metal is brought into contact with a semiconductor the electrical behaviour at the junction either takes the ohmic or Schottky characteristics. However, this device type is asymmetrical in nature in the sense that the Schottky junction is only one-sided. Figure 14.5 shows the band diagram of a metal and an n-type semiconductor before and after equilibrium.

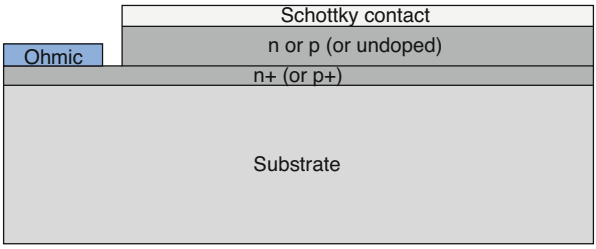

Fig. 14.4 Metal-semiconductor Schottky contact

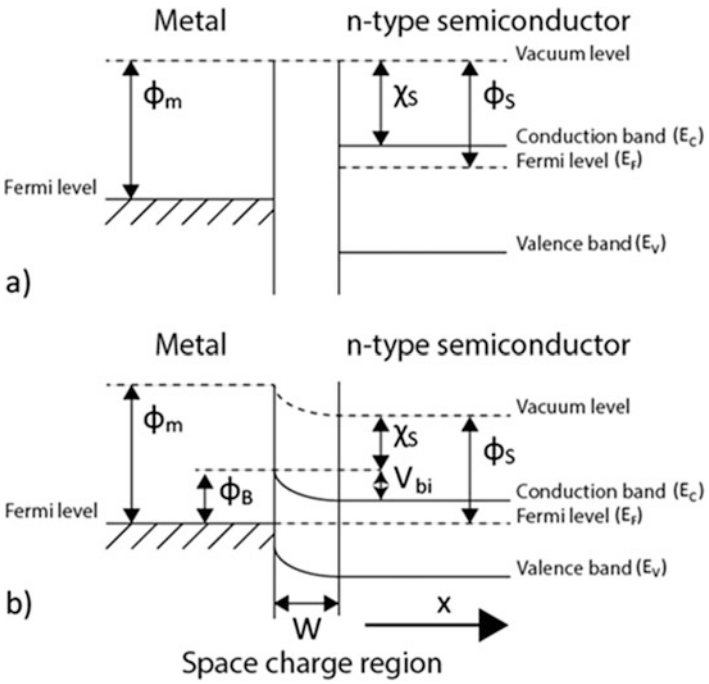

Fig. 14.5 Band diagram of a metal and n-type semiconductor: (**a**) before equilibrium and (**b**) after equilibrium

In the above figure, χ_s is the semiconductor electron affinity, ϕ_s is the semiconductor workfunction, ϕ_m is the metal workfunction, ϕ_B is the Schottky barrier height, V_{bi} is the built-in voltage and W is the space charge region (SCR) width along the distance x. Figure 14.5a shows the Fermi levels of the metal and semiconductor before equilibrium is reached. Upon contact between the two materials, the Fermi energy level becomes constant throughout the structure reaching an equilibrium. This is thanks to a flow of electrons from the semiconductor into the lower energy states of the metal leaving positively charged ions behind, thus creating a depletion region (SCR). It should be noted that Fig. 14.5b assumes the metal workfunction to be larger compared to that of the semiconductor else an ohmic contact will be the result. For p-type semiconductors this is the opposite. Table 14.2 summarizes the requirements for Schottky and ohmic contacts for both semiconductor types. Table 14.3 lists the work functions of several metals and the resulting barrier height for 4H-SiC having an electron affinity of 3.3 eV.

As a result of the shown band bending, a potential barrier ϕ_B known as the Schottky barrier is seen by the electrons in the metal side trying to move to the semiconductor. Ideally, the Schottky barrier height is given by

$$\phi_B = \phi_m - \chi_s \tag{14.6}$$

The equation shows the Schottky contact dependence on the semiconductor electron affinity (χ_s) and the metal workfunction (ϕ_m) $\cdot$ χ_s is given by

$$\chi_s = \phi_s - (E_c - E_f) \tag{14.7}$$

Table 14.2 Schottky contact workfunctions requirement

Semiconductor	Schottky (rectifying)	Ohmic
n-type	$\phi_m > \phi_s$	$\phi_m < \phi_s$
p-type	$\phi_m < \phi_s$	$\phi_m > \phi_s$

Table 14.3 Relevant metals and their workfunctions

Metal	Workfunction (ϕ_m) eV	Barrier height 4H-SiC (ϕ_m) $_{eV}$
Au	5.10	1.80
Ag	4.26	0.96
Al	4.28	0.98
B	4.45	1.15
Cr	4.50	1.20
Cu	4.65	1.35
Ni	5.15	1.85
Pt	5.65	2.35
W	4.55	1.25

On the other hand, after the band bending the electrons from the semiconductor side will also see a built-in potential barrier known as the built-in voltage V_{bi} given by

$$V_{bi} = \phi_m - \phi_s = \phi_B - (E_c - E_f) \tag{14.8}$$

As discussed before, the semiconductor should be low doped to achieve Schottky barrier behaviour. The reason behind this is the dependence of the built-in voltage on doping similar to the pn-junction. This dependence is shown below equations.

$$E_c - E_f = \frac{k_B T}{q} \ln\left(\frac{N_c}{N_d}\right) \tag{14.9}$$

Yielding

$$V_{bi} = \phi_m - \chi_s - \frac{k_B T}{q} \ln\left(\frac{N_c}{N_d}\right) = \phi_B - \frac{k_B T}{q} \ln\left(\frac{N_c}{N_d}\right) \tag{14.10}$$

where k_B is the Boltzmann's constant, T is the temperature and N_d is the donor concentration. The built-in voltage is the barrier seen by electrons in the semiconductor which prevents further flow of electrons into the metal. N_c is the effective density of states in the conduction band and is given by

$$N_c = 4\sqrt{2}\frac{\sqrt[3]{\pi m^* k_B T}}{h^3} \tag{14.11}$$

where m^* is the effective electron mass and h is the Planck's constant ($h = 6.63 \cdot 10^{-34}\ m^2 \cdot kg \cdot s^{-1}$). Using the above equation for the built-in voltage, a graph can be constructed for the dependence on the doping concentration of n-type 4H-SiC, see Fig. 14.6.

The above figure assumes Nickel is used as a Schottky metal contact at a temperature of 300 K. To calculate the effective density, the anisotropic nature of the 4H-SiC needs to be considered since the effective mass varies for different crystal orientations.

When a Schottky contact is biased, either reverse or forward, the barrier height will change as shown in Fig. 14.7a, b.

The electrons in the semiconductor will easily diffuse across the SCR into metal for a sufficiently reduced barrier height due to forward bias ($V_{bi} - V_F$). On the other hand, for $V_{bi} + V_R$ the barrier will be increased blocking the electrons. Furthermore, the above diagrams are very similar to those of a pn-junction resulting in similar *I-V* characteristics with exponential behaviour. However, the current mechanism in the MS junction is due to the flow of majority carrier electrons as opposed to the pn-junction, allowing for high-speed operation. The high speed is also thanks to the one-sided depletion region of the Schottky diode. Similar to a pn-junction the

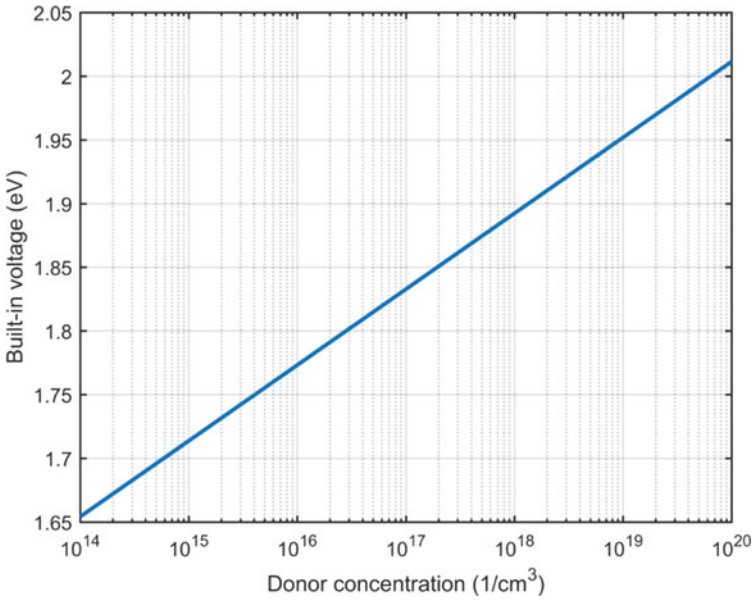

Fig. 14.6 Built-in voltage as a function of the donor concentration in the n-type semiconductor

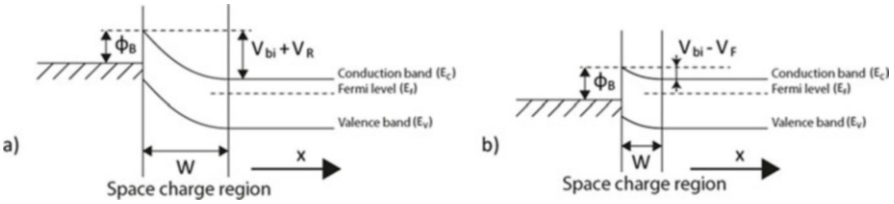

Fig. 14.7 Ideal band diagram of a metal and n-type semiconductor: (**a**) under reverse bias and (**b**) under forward bias

electrostatic properties, the electric field and SCR width, can be determined starting with Poisson's equation. Consider

$$\frac{dE}{dx} = \frac{\rho(x)}{\epsilon_0 \epsilon_r} \tag{14.12}$$

where $\rho(x)$ is the SCR volume density and $\epsilon_0 \epsilon_r$ is the permittivity of the semiconductor. Integrating the above equation yields

$$E = \int \frac{qN_\mathrm{d}}{\epsilon_0 \epsilon_r} dx = \frac{qN_\mathrm{d}x}{\epsilon_0 \epsilon_r} + C_1 \tag{14.13}$$

To solve for the integration constant, assume electric field at the SCR edge of the semiconductor to be zero.

$$C_1 = \frac{qN_d x}{\epsilon_0 \epsilon_r} \tag{14.14}$$

Assuming the SCR starts at $x = 0$ and extends to $x = W$, the electric field at any point y in the x-direction can be written as

$$E = -\frac{qN_d (W - x)}{\epsilon_0 \epsilon_r} \tag{14.15}$$

The SCR width can be determined by assuming a highly doped p layer to represent the metal in a p^+n junction. The SCR in the n-type semiconductor under a reverse bias then becomes

$$W = \sqrt{\frac{2\epsilon_0 \epsilon_r (V_{bi} + V_R)}{qN_d}} \tag{14.16}$$

It should be noted that the photogenerated e-h pairs outside the SCR will recombine before reaching the electrodes. Charge carriers generated in the SCR will be collected at the electrodes before recombination takes place. Now that the single junction contact is introduced, this can be extended with a second contact. Consider Fig. 14.8a, b showing the MSM band diagram after equilibrium and the back-to-back diodes.

As can be seen from the above figure, the two contacts to the semiconductor are symmetrical of nature. However, when a bias is applied to the device this symmetry is broken where one barrier height is increased, and the other is lowered. This results in an operation where one diode is always reverse biased and the other forward biased allowing the flow of charge carriers to form a current in an external circuit. As a consequence, the MSM Schottky device will exhibit nonlinear I-V characteristics. This method allows for a low dark current, hence the minimum detectable signal

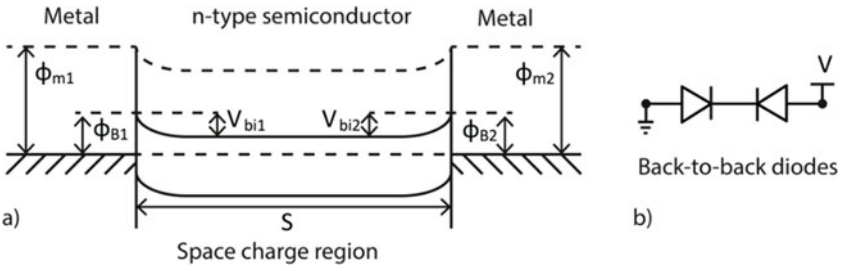

Fig. 14.8 (**a**) MSM band diagram after equilibrium and (**b**) MSM back-to-back diodes

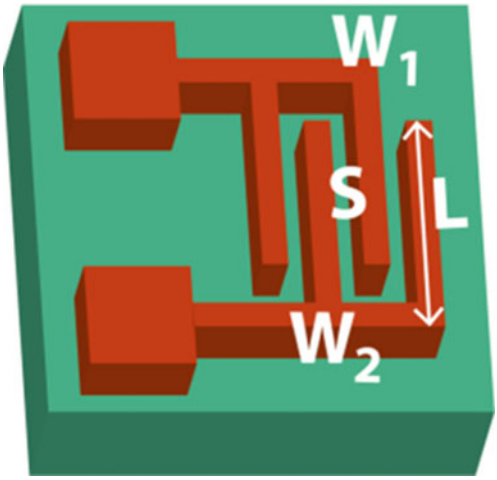

Fig. 14.9 MSM structure

capability is enhanced. Of course, to keep the dark current as low as possible, the crystal quality of the semiconductor should be as high as possible while the metal selected should result in an as high as possible barrier height [17]. This can also result in higher responsivities. Similar to the single Schottky contact, high speeds can be achieved thanks to the low junction capacitance and high BW is available. Further the simple structure is CMOS compatible while allowing also for less conventional processes such as the addition of nanomaterials for enhancing the device responsivity usually found in photoconductive devices. Consider Fig. 14.9 illustrating an MSM device where L is the length of a single finger electrode, S is the separation between the opposing electrodes, and W_1 and W_2 are the widths of the top and bottom finger electrodes, respectively.

The reason for having two electrode widths is enabling asymmetry by geometrical design to enhance the performance of the device. Changing both electrode width can also have a significant influence on the performance similar to increasing the bias voltage [18]. An Au/ZnO MSM device was designed with two electrode widths where one electrode was fixed and the other decreased [19]. The device showed at a ratio of 20:1 an enhancement in the responsivity from 0.3 to 20 mA/W at the same conditions while operating in photovoltaic mode at 0 V as a self-powered device. Moreover, the device showed an enhanced operation speed. The effect of electrodes asymmetry was explained as a strong influence on the electrical field distribution built in the Schottky junction where the electrical field can prevent the recombination of photogenerated e-h pairs and separate the photogenerated carriers more efficiently.

14.2.3 MS Schottky Contact Current Mechanism

The current mechanisms in Schottky contact devices is due to three main mechanisms: thermionic emission (TE), thermionic field emission (TFE) and field emission (FE) [17]. Figure 14.10 illustrates these effects.

Thermionic emission describes the electron flow over the potential barrier when the charge carriers gain enough thermal energy while assuming the barrier height to be larger than the thermal voltage (k_BT/q). This is dominant in moderately doped semiconductors operating at room temperature and is used to describe the *I-V* characteristics of the MS Schottky contact.

The current density given by TE is according to Eq. (14.17).

$$J = J_s\left(\exp\left(\frac{qV}{k_BT}\right) - 1\right) \tag{14.17}$$

where V is the applied voltage. The saturation current J_s is given by

$$J_s = A^{**}T^2 \exp\left(-\frac{q\phi_B}{k_BT}\right) \tag{14.18}$$

where A^{**} is the effective Richardson constant. This equation allows for the calculation of the barrier height using the *I-V* characteristic of a MS Schottky device. J_s is found experimentally.

Thermionic field emission results from high electric field application to the semiconductor under temperatures relatively higher than room temperature. As a result, the current density due to this mechanism will be higher as compared to TE and FE mechanisms.

Field emission, also known as quantum tunnelling, is due to the narrowing of the potential barrier as a result of high electric field giving the electrons a higher probability of tunnelling through the barrier. This mechanism is more dominant

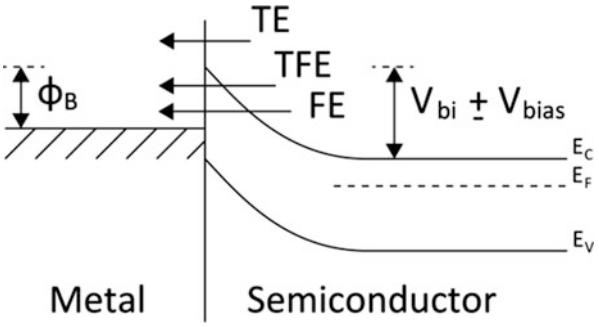

Fig. 14.10 Schottky contact current mechanisms

for high doping concentrations in the semiconductor or at low temperatures. The tunnelling current is given by

$$J_t = J_{ts} \exp\left(-\frac{q\phi_B}{E_{00}}\right) \tag{14.19}$$

where J_{ts} is the tunnelling saturation current and E_{00} is the characteristic tunnelling energy related to the tunnelling effect transmission probability. E_{00} is given by

$$E_{00} = \frac{qh}{4\pi}\sqrt{\frac{N_d}{\epsilon_s m^*}} \tag{14.20}$$

This parameter helps predict which mechanism will be dominating depending on three conditions given by the ratio E_{00}/k_BT as shown by

$$\text{Condition 1} : \frac{E_{00}}{qk_BT} \leq 0.2 \tag{14.21}$$

$$\text{Condition 2} : 0.2 < \frac{E_{00}}{qk_BT} \leq 5 \tag{14.22}$$

$$\text{Condition 3} : \frac{E_{00}}{qk_BT} > 5 \tag{14.23}$$

From these equations, it should be possible to calculate at room temperature and see that TE dominates at $N \leq 3 \times 10^{17}\text{cm}^{-3}$ and TFE at $3 \cdot 10^{17}\text{cm}^{-3} \leq N \leq 2 \cdot 10^{20}\text{cm}^{-3}$. At higher doping levels, FE becomes dominant. Recombination in the SCR and recombination in neutral region under forward bias also contribute to the current. In this work TE is considered since low doped semiconductors are used for the fabrication of the MSM Schottky devices. There are other effects in the device associated with the metal-semiconductor contact. Such can be the image-force, interface layers, traps and other defects, etc. Such effects may be discussed when relevant for the characterization of the device.

14.2.4 PN-Junction Photodiode

The pn-junction photodiode is one of the first junction semiconducting devices created. It is a simple structure consisting of a p-type layer on top of an n-type layer or substrate. By bringing the two-layer types a potential barrier exists under equilibrium and no net current flow through the diode exists. Figure 14.11 shows an illustration of the device along with its electrical symbol.

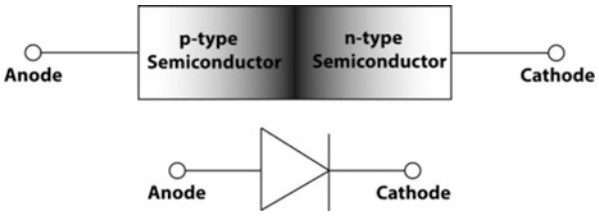

Fig. 14.11 PN-junction diode illustration and its electrical symbol

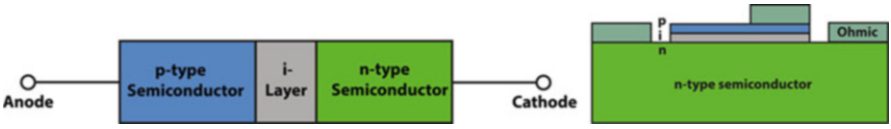

Fig. 14.12 Pin-junction diode illustrations

The device has a response to incident photons in the form of free charge carriers generation. Each incident photon generates an e-h pair which are separated by an electrical field generated by reverse biasing the device. Here the electrons at the p-side move through the depletion region towards the n-type side while the holes at the n-type side move towards the p-type side for collection resulting in a small electric current.

The pn-junction has drawbacks. The first drawback is a large dark current restricting low light level detection. The depletion region of the device is essentially a capacitor which is too large due to the small width of the SCR. This results in limiting fast response detection and high frequency modulation. Another disadvantage is a low QE at long wavelengths, although this is not an issue in this work for the application of UV sensing.

14.2.4.1 Pin-Junction Photodiode

To overcome some of the limitations associated with the pn-junction, an intrinsic layer is added between the p- and n-type layers as shown in Fig. 14.12.

The depletion region is enhanced by the width of the intrinsic layer. First this can be tailored to reduce the capacitance of the junction for the same optical sensing area enabling faster response and higher frequency modulation with bandwidths typically in the range of 10 MHz. The capacitance is then typically in the order of pF. This is because the capacitance of the device becomes bias independent as shown in Eq. (14.24).

$$C = \frac{\varepsilon_0 \varepsilon_r A}{W} \tag{14.24}$$

Thanks to low doping of the layer the electrical field becomes uniform which also presents further diffusion of charge carriers and enables lower noise [2]. Moreover, the SCR becomes nearly independent of the applied bias which is beneficial for a stable operation and an increased breakdown voltage V_{br}. The QE of the device is also enhanced through the tailoring of the intrinsic layer. Here the photons are mostly absorbed in the intrinsic layer. It should be noted that even though more e-h pairs can be generated for a larger W, this will also result in a slower response as shown in Eq. (14.25).

$$T_{drift} = \frac{W}{V_d} \tag{14.25}$$

This is because the transit time of the photogenerated charge carriers will reduce the response time of the photodiode. This results in a trade-off between speed and responsivity of the device due to reduced photon absorption at smaller W.

For the ohmic contacting to the layers additional n^+ and p^+ layers can be used as a connection to the metals for low contact resistances [2]. This property also results in a usually higher detectivity compared to Schottky photodiodes mainly due to their lower dark current (related to noise) [13]. Next to this depending on the specific design, responsivity can be significantly increased at reverse voltages in Schottky and p-n photodetectors [13]. However, the increased bias also reduces the UV-to-visible ratio.

This type of device has been used in various research and showed good performance. A 6H-SiC UV pin-junction photodetector is already commercially available [20]. Here the n^+ layer is always doped with large dose typically $>10^{19}$ cm^{-3} where the devices showed an extremely low reverse current, and a peak responsivity of 150–175 mA/W range at 270 nm, corresponding to a 70–85% quantum efficiency. Another work showed a 4H-SiC based pin PD was designed to have a responsivity of 0.13 A/W at a wavelength of 270 nm, an EQE of ~61% and a UV-to-visible ratio exceeding 10^3 for the wavelength of 270 and 380 nm. The PDs usually require passivation which is done by coating with SiO_2 layer for passivation and antireflection where the SiO_2 layer has an absorption at $\lambda < 200$ nm [5, 21]. However, surface recombination plays an important role especially for far UV photodiodes [5]. Thus, the control of the semiconductor to SiO_2 interface is important for the design [5]. The thickness of the SiO_2 layer should also be as thin as possible to improve the penetration depth of the photons with higher energy which can be the case for VUV photodiodes [5]. In another research, the performance of a p-n device was improved without the need of this passivation layer. Here a 4H-SiC pn-junction UV photodetector was designed and achieved a responsivity of 0.03 A/W at 280 nm. The photocurrent was found to be four orders of magnitude larger than the dark current [22].

Since the pin photodiode is a multi-layer device, some care should be taken into the design. The absorption losses in the field-free layers should be avoided as much as possible. This can be accomplished by using very thin p- and n-layers. Furthermore, when selecting a wide bandgap for the doped top layer, it should have

an absorption in a spectral range which allows for light absorption in the intrinsic layer.

14.2.5 The Avalanche Photodiode

An important disadvantage of the pn and pin-junctions is the lack of gain, i.e. a successfully absorbed photon only generates a single e-h pair. Amplifying the output signal using an external gain will add a significant amount of noise which will drown weak signals of very low optical input signal. In the past other type of devices were used for this, e.g. a photomultiplier (PMT), i.e. a vacuum tube which has the high sensitivity requirement. However, the PMT has a bulky design, low QE, limited linearity, a narrow spectral operation region and generates heat. The limitations of the PMT and pin photodiodes can be overcome using a pin photodiode designed to have internal gain, also known as avalanche gain, hence the name avalanche photodiode (APD).

To achieve the internal gain, a large reverse bias voltage is applied to the pin diode near the breakdown voltage of the junction. The pin device is however modified to achieve this result by adding a thin layer of p-type doped material between the intrinsic and n-type layers as illustrated in Fig. 14.13. Here the electrical field is shown to be maximum at the pn^{+}-junction.

The increased reverse bias allows for a higher electric field close to the junction breakdown enabling impact ionization [2]. Each time a photon is absorbed it will generate an e-h pair. The electric field then accelerates the electron which gains enough kinetic energy to cause impact ionization resulting in an avalanche multiplication of electrons, e.g. an internal gain is obtained. The APD knows some adaptations which include heterostructured devices and multi-quantum well. The APD presents many advantages such as high speed, high sensitivity, high

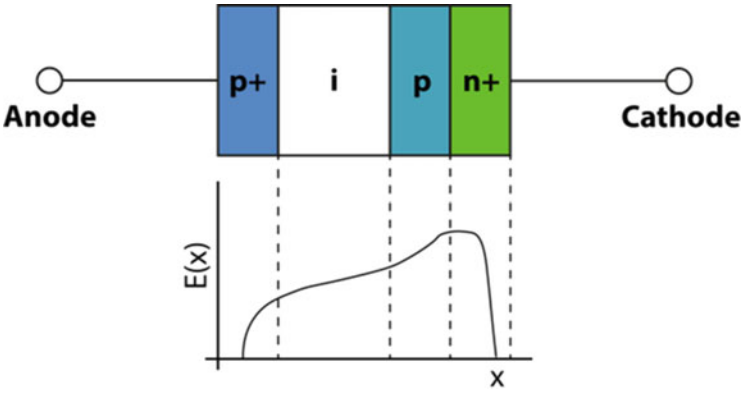

Fig. 14.13 Avalanche pin-junction illustration and the electrical field across the layers

responsivity, high internal gain and even low noise. For example, 4H-SiC APDs exhibit low noise thanks to the large ionization coefficient ratio of ∼10 between holes and electrons [5, 23]. The APD can also be based on other types of junctions such as the MS junction [2] but is by far based on the pin-junction. The latter shows trade-offs between the maximum achievable responsivity, speed and operating voltage [2, 23].

Of course, the APD also has disadvantages. The multiplication effect not only results in a higher photocurrent, but also in a higher dark current and lower noise performance while also adding noise from the multiplication process itself. The bandwidth of the device becomes smaller while the response time increases due to the avalanche build-up time and holes transit time through the absorption region.

The devices can be improved using various techniques. A pin-junction photodetector was fabricated and showed a dark current density of 63 nA/cm^2 at 90 pA, a QE of 40% and a gain of 10^3. The same device was optimized using a recessed-window structure and by improving the antireflection (AR) coating layer [24]. The work showed a responsivity of 136 mA/W at 262 nm, with an EQE of 60%, avalanche gains of over 10^6, an excess noise factor characterized by k value of ∼0.1, and a spatially uniform response [25]. The pin-junction device performance can be further improved by using a separate absorption and multiplication (SAM) structure [23]. A SAM-APD has separate high-field multiplication and absorption regions and by optimizing the thicknesses and doping concentrations of these layers, some of the issues associated with the pin-structure APD can be solved [23]. For instance, the SAM-APD structure injects only a single type of carrier into the multiplication region which reduces the multiplication noise that arises from the stochastic nature of the multiplication process [23]. The fabricated device achieved an optical gain higher than $1.8 \cdot 10^4$ at 90% of the breakdown voltage of about 55 V. At 42 V reverse bias and 270 nm wavelength, the peak responsivity increased to 0.203 A/W, corresponding to a maximum EQE of ∼93% [23].

14.3 Operation Modes

14.3.1 Photovoltaic Mode

The photodetectors can be operated in either the photovoltaic (PV) or photoconductive (PC) modes. Devices based on Schottky barrier and p(i)n junctions such as diodes and transistors have been applied using the PV mode [11]. In the PV mode the diode is operated in open circuit similar to a photocell, without an external bias. When the optical active area is illuminated, the equilibrium at the junction is disturbed causing e-h pairs to be generated at the depletion region. The electric field across the junction then separates charge carriers by pulling the electrons towards the n-side and holes towards the p-side. Then a current flows through the diode from the n- to the p-side. As the barrier further decreases more charge carriers can cross

this and an increase in the forward current. The forward current is then balanced out by the photocurrent so that no net current can flow. The barrier lowering is then seen as a measurable voltage across the open circuited device.

The governing equations of the photovoltaic mode are then started with equating the forward- and photocurrents as shown below.

$$I_{\mathrm{f}} = I_{\mathrm{ph}} \tag{14.26}$$

with

$$I_{\mathrm{ph}} = I_0 \left(\exp\left(\frac{qV}{k_{\mathrm{B}}T} \right) - 1 \right) \approx I_0 \exp\left(\frac{qV}{k_{\mathrm{B}}T} \right) \tag{14.27}$$

The above equation assumes the exponential term to be much greater than unity. The open circuit voltage is then given by

$$V = \frac{k_{\mathrm{B}}T}{q} \ln\left(\frac{I_{\mathrm{ph}}}{I_0} \right) \tag{14.28}$$

Notice that the voltage is a nonlinear function of the current, hence also the illumination. This readout method has a slow response which depends on the absorbing layers thickness. However, a major advantage is the lack of dark current, hence lower noise, thanks to the absence of biasing.

14.3.2 Photoconductive Mode

The photodiodes can be operated in PC mode by applying a reverse voltage bias. Here the n-side is connected to the positive terminal while the p-side is connected to the negative terminal. The electric field separates the electrons and holes in the depletion region widening it further and increasing the energy barrier height. Thanks to this the flow of charge carriers is almost completely stopped and only a small reverse current still flows, also known as a dark current, I_{d}. This current is the result of thermally generated charge carriers which is always present for temperatures $T > 0$ K.

As the device absorbs incident photons, extra charge carriers are generated and separated by the electric field in the depletion region. This results in a photocurrent I_{ph} in the same direction as the dark current.

Every method knows advantages and disadvantages. The output signal to be measured is the photocurrent which is a linear function of the illumination as compared to the open circuit voltage for the PV mode which is nonlinear. The PC mode also results in a higher response as compared to the PV mode. Since the reverse biasing results in a higher electric field across the depletion region widening the depletion region, the response speed is also enhanced as the transit time for the

charge carriers is reduced. Of course, the electrical biasing results in an increased noise due to the dark current.

14.4 Photodetector Characteristics

Standard metrics of photodetectors have been defined to describe the performance of photodetectors. This enables the selection of devices for the appropriate applications. This section will describe the relevant parameters used for characterizing the photodetectors.

14.4.1 Photoconductive Mode

The incoming photons incident on the optical active area of the photodetector are not all collected or converted to e-h pairs. To describe this, the quantum efficiency (QE) is defined as the ratio of the number of generated electrons to the number of incident photons [2, 5]. This is given by

$$\eta = \frac{\#\text{of generated electrons}}{\#\text{of incident photons}} \times 100\% \tag{14.29}$$

The QE can then be related to the responsivity (R), defined as the ratio of the photocurrent and the incoming optical power with the unit A/W [2], given by

$$\eta = \frac{I_{\text{ph}}/q}{P_{\text{opt}}/h\nu} = \frac{R \cdot h\nu}{q} = R \cdot \frac{hc}{\lambda q} \rightarrow R = \frac{I_{\text{ph}}}{P_{\text{opt}}} = \frac{\eta\lambda q}{hc} \tag{14.30}$$

where ν is the frequency, c is the speed of light and λ is the wavelength of interest. The above equation also shows that the responsivity is a linear function of the wavelength and that even though photons at shorter wavelengths have more energy, the responsivity will be lower [2, 5, 11].

$$R = \frac{\eta\lambda q G}{hc} = \frac{\eta\lambda G}{1240} \quad [\text{nm}] \tag{14.31}$$

The responsivity further also depends on photoconductive gain G and the frequency modulation. Here G is equal to unity for diodes without multiplication or defect enhanced to trap carriers and generate gain by $\tau_{\text{lifetime}}/\tau_{\text{transit}}$.

$$R = \frac{\eta\lambda G}{1240} \cdot \frac{1}{\sqrt{1 + (2\pi f\tau)^2}} \tag{14.32}$$

where the 3 dB frequency is at $1/\sqrt{2}$ of the responsivity value under illumination. It should be noted that a gain increase will reduce this value. As a result of reflection at the IDT contacts of the device, the QE is reduced and is characterized by the fill factor given by

$$F = \frac{W}{S + W} \tag{14.33}$$

where W is the width of an individual finger electrode and S is the separation between opposing finger electrodes. For asymmetrical design, this factor changes. This figure can be enhanced when semitransparent electrodes are used, e.g. Indium Tin Oxide (ITO) or graphene electrodes.

14.4.2 UV-to-Visible Discrimination Ratio

The UV-to-visible is also a figure of merit which is defined as the ratio between the peak responsivity and that below the bandgap, thus the UV-to-visible ratio [13]. This ratio is an indication of the quality of the layer and can be defined as the number of nm needed to reduce the responsivity by a decade as is indicative for electrical filters [13].

14.4.3 Spectral Response/Operation Region

The spectral response is associated with the cut-off wavelength which is often given as an indication of the operating point or region of a photodetector [2]. The spectral cut-off wavelength can be defined as the wavelength for which the responsivity drops by either 10 or 50%. This also classifies the photodetector as visible-blind, solar-blind, etc.

14.4.4 Signal-to-Noise Ratio

One of the most important figures of merits is the signal-to-noise ratio (SNR) which describes how good the signal can be distinguished from the noise. There are several noise contributions imposed on the output signal of the photodetector which will be discussed in the coming text. The SNR is given by Eq. (14.34).

$$\text{SNR} = \frac{I_{\text{ph}}^2}{I_{n,\text{total}}^2} \tag{14.34}$$

In the case of a high photocurrent, the above equation can be approximated by:

$$\mathrm{SNR} \approx \frac{I_{\mathrm{ph}}^2}{I_{n,\mathrm{s}}^2} \tag{14.35}$$

where only the shot noise is taken into account. Here it shows that the lowest detectable power is SNR = 1.

14.4.5 Signal-to-Noise Ratio

Next to the SNR the noise equivalent power (NEP) is also specified for photodetectors as a figure of merit. The NEP is defined as the ratio of the noise current to the responsivity R. The NEP, expressed in Watt, is usually calculated at the wavelength of interest at a BW of 1 Hz and room temperature. Further the parameter can be normalized for the BW [5] by

$$\mathrm{NEP}^* = \frac{\mathrm{NEP}}{\sqrt{\mathrm{BW}}} \tag{14.36}$$

However, the NEP is not adequate for comparing different types of photodetectors as this is dependent on parameters such as area, temperature, biasing voltage and modulation frequency. To enable comparison between different device types, the devices should be independent of the area A and BW [2, 5, 13]. This value is used to show the minimum detectable optical power of a photodetector which is limited by various noise sources and can be from the detector properties, readout setup such as the noise in an amplifying transistor, or from the statistical fluctuations of the optical signal and any significant background radiation during the detection process [2]. The detectivity D is given by

$$D = \frac{1}{\mathrm{NEP}} \tag{14.37}$$

and is independent of area A and BW by

$$D^* = \frac{\sqrt{\mathrm{ABW}}}{\mathrm{NEP}} \tag{14.38}$$

expressed in $\mathrm{cm}\sqrt{\mathrm{Hz}}/\mathrm{W}$ or Jones with typical values around $10^{11} - 10^{13}$ Jones or even higher for high end photodetectors such as single photon detectors (SPAD). This shows that it's important to consider all the aspect of the measuring system including the photodetector type and design but also the readout components [2].

Thus any noise contributions from the readout circuit should be kept to a minimum when designing for high speed and precision applications.

14.4.6 Minimum Detectable Optical Power

The signal of interest which can be seen by the photodetector has two limits: (1) an upper limit at which the signal detection is determined by the maximum current that the detector can handle without becoming saturated and (2) a lower limit set by the noise floor. The minimum output current signal will then be

$$\text{Noise floor} = \frac{\text{Total noise } (A)}{\text{Responsivity } (A/W)} \tag{14.39}$$

To gain an idea of what the noise sources are, consider below figure. The noise sources associated with photodetectors are thermal, shot, 1/*f*, and photon noises.

Thermal noise, also known as Johnson noise, is encountered in resistive materials for temperatures higher than 0 K. The contributions are from the shunt resistor of the photodetector and any other resistances encountered by the output current signal such as the series resistances and load resistance to convert the current to a voltage. The noise is the result of thermal energy generating charge carriers in conducting materials. Here the electrons are constantly randomly moving and colliding with the atoms of the material. Each collision then contributes to the noise current. However, the sum of all these contributions is zero and thus no net current can flow. This is given by

$$I_{n,t} = \sqrt{\frac{4K_{\mathrm{B}}T\mathrm{BW}}{R}} \tag{14.40}$$

where K_{B} is the Boltzmann constant, T is the temperature, BW is the operating bandwidth and R is the resistance. Notice that this noise can be reduced by cooling the system, operating at a lower BW or reducing the resistances. Operation at a lower BW is not straightforward as the 1/*f* noise dominates. Reducing the load resistance will reduce also the strength of the converted signal.

The shot noise arises from fluctuations in the stream of electrons towards the electrodes. This was first derived from vacuum tube technology. The noise is also referred to as generation-recombination (g-r) noise. The shot noise is given by

$$I_{n,\mathrm{s}} = I_{\mathrm{sat}}\left(\exp\left(\frac{qV}{K_{\mathrm{B}}t}\right) - 1\right) = -I_{\mathrm{d}} \tag{14.41}$$

with I_{sat} being the reverse saturation current. For dark current I_d the noise becomes

$$i_d^2 = 2q\ \mathrm{BW} I_d \tag{14.42}$$

As for the case when there is illumination (quantum noise), the equation becomes

$$i_d^2 = 2q\ \mathrm{BW} I_{ph} \tag{14.43}$$

The shot noise can be minimized by minimizing the DC component of the current (dark current). This can be further minimized by keeping the application BW as low as possible, at 1 Hz as is commonly done. Later in this text the signal-to-noise ratio (SNR) will be shown where the shot noise can be used as an estimate of the lower limit of the noise when the photocurrent is sufficiently large.

The 1/*f* noise, also referred to as excess noise, is due to a number of effects such as contacts and surface trap states but is not well understood. Thus, by good contact fabrication and reduction of surface traps this noise may be reduced. The 1/*f* noise is inversely proportional to the frequency and is given by

$$I_f^2 \sim \frac{I^2 \mathrm{BW}}{f} \tag{14.44}$$

With f being the frequency, as shown in Fig. 14.14 this noise is large at low frequencies and can be reduced if f is sufficiently large, usually >1 kHz for photodetectors.

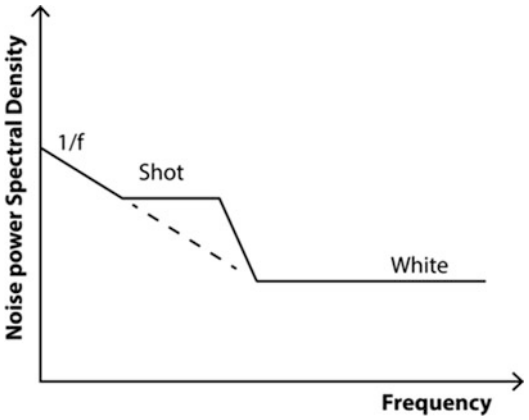

Fig. 14.14 Noise sources

14.4.7 Optical Absorption Coefficient

The absorption coefficient (α) indicates the capability of a material to absorb photons with the enough energy. A material through which electromagnetic waves can travel without loss of energy is transparent. On the other hand, when electromagnetic waves are completely reflected (or absorbed), they are called opaque. Semiconductors are semitransparent which means that electromagnetic waves can possibly travel through the material while an attenuation of the intensity occurs. Electromagnetic waves penetrating into a semiconductor will travel into the material for a length of $1/\alpha$, also referred to as penetration depth. This means that the absorption material should have a thickness at least larger than the penetration depth. The coefficient allows for determining the number of photogenerated free charges (e-h pairs) which can be generated at a spectral range and what the attenuation is of the optical power P for different depths [2]. This is defined by Eq. (14.45) as

$$\alpha_{\text{opt},i}(\lambda) = \frac{4\pi\kappa_i(\lambda)}{\lambda} \tag{14.45}$$

Figure 14.15 shows the spectra of absorption coefficients at room temperature for various direct and indirect semiconductors [2].

As can be seen 4H-SiC has an absorption in the UV range while it has a strong attenuation at longer wavelengths (smaller bandgap).

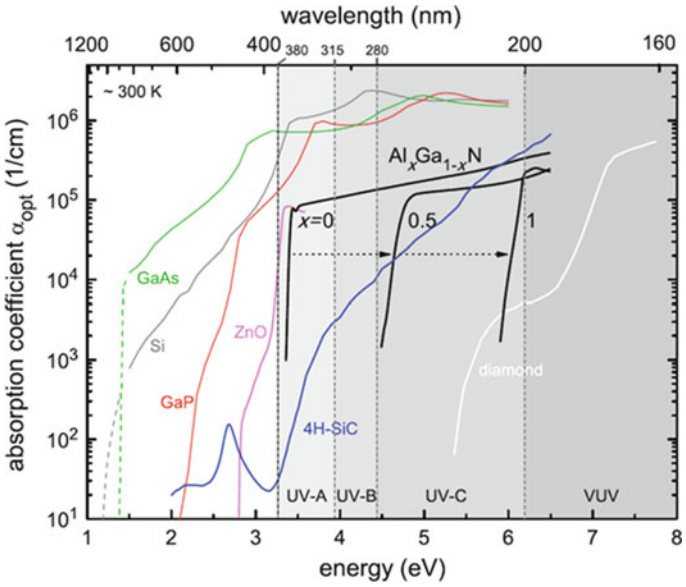

Fig. 14.15 Optical absorption coefficient for various semiconductors. Source [2]

14.4.8 Response Time and Persistent Photoconductivity

Response time gives the operation speed of a photodetector in terms of rise and fall times. Here both the rise and fall times are used and are defined as the time it takes for the detector to detect a rectangular light pulse excitation and have its response go from 10 to 90% of its value, and vice versa as is shown in Fig. 14.16 [2, 5].

The response time is determined by a number of factors which limits the bandwidth of the photodiode operation. The contributions can be from:

- The series resistance and the capacitance of a junction which give the RC time.
- The drift of photogenerated carriers in high-field regions such as the intrinsic layer in a pin photodiode which gives the drift time.
- The diffusion of photogenerated minority carriers in field-free regions such as the p- and n-regions in a pin photodiode which gives the diffusion time.

The times from each contribution are then added as a square and taken square root of the total value. Some photoconductors may show large rise and fall times which may be even in excess of several 1000 s [2]. Such phenomena are known as persistent photoconductivity (PPC) and may render photodetectors non-useful for many applications such as corona discharge where the frequency of the plasma is two times the net-frequency at 100 Hz or 120 Hz. These phenomena are often found to let itself be described by a stretched exponential of the form [2]

$$I(t) \sim \exp\left(-\frac{t}{\tau}\right)^{\beta} \tag{14.46}$$

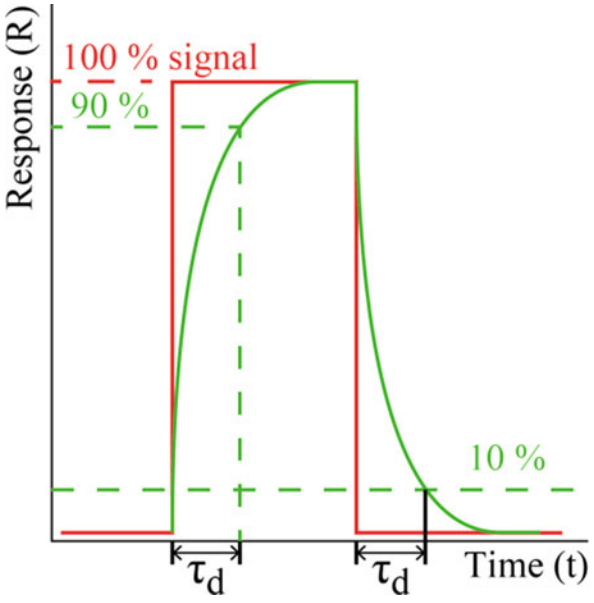

Fig. 14.16 Rise and fall times for a square optical signal

where τ is a time constant and $0 < \beta \leq 1$ is the Kohlrausch stretching parameter. The latter accounts for the microscopic nature of the electronic and atomic relaxation processes underlying the non-exponential change in measured conductivity [2].

14.4.9 Bandwidth

Bandwidth (BW) is defined as the frequency at which the photocurrent is (3 dB) lower than the low-frequency value [5]. This can be related to the decay time (τ) for the special case of exponential transient response by

$$\mathrm{BW} = \frac{1}{2\pi\tau} = \frac{2.20}{2\pi\tau_{\mathrm{d}}} = \frac{2.20}{2\pi\tau_{\mathrm{r}}} \tag{14.47}$$

As was shown in Fig. 14.16, to get a reliable result for the bandwidth, the excitation pulse needs to be rectangular with a rise time much shorter and pulse width much larger than the rise time of the response, respectively. This is required in order for the photocurrent to reach a steady state value [5].

14.4.10 Linearity

The linearity between the photocurrent and the optical power incident on the active area of the device is an important property which allows for a power-independent responsivity (R_{sp}) as given by Eq. (14.31) and a reliable device operation [2]. The linearity is affected by a number of processes such as the carrier recombination kinetics in the absorber material, the equivalent electrical circuit of the photodetector and the readout circuit [2].

14.4.11 Dynamic Range

The dynamic range gives the range over which the detector response is linear with respect to the incident light intensity [11].

14.5 Final Remarks

Optical detections are required in many applications, ranging from civil to military fields. Depending on the optical source, each sensing element needs to have distinct properties with the spectral range at the top. Choices such as sensitivity and

environment play an equally important role, if not more important. The properties of the sensors can be tailored by selecting a proper material for a proper photodetector device type. In this chapter, photodetection principles and requirements are discussed, including design considerations and relevant parameters.

References

1. L. Sang, M. Liao, M. Sumiya, A comprehensive review of semiconductor ultraviolet photodetectors: from thin film to one-dimensional nanostructures. Sensors **13**, 10482 (2013)
2. M. Kneissl, J. Rass, III-nitride ultraviolet emitters, in *Springer Series in Materials Science* (Springer, 2016)
3. H. Chen, K. Liu, L. Hu, A.A. Al-Ghamdi, X. Fang, New concept ultraviolet photodetectors. Mater. Today **18**, 493 (2015)
4. A. Aldalbahi, E. Li, M. Rivera, R. Velazquez, T. Altalhi, X. Peng, P.X. Feng, A new approach for fabrications of SiC based photodetectors. Sci. Rep. **6**, 23457 (2016)
5. E. Monroy, F. Omnès, F. Calle, Wide-bandgap semiconductor ultraviolet photodetectors. Semicond. Sci. Technol. **18**, R33 (2003)
6. L. Luo, Y. Zhang, S.S. Mao, L. Lin, Fabrication and characterization of ZnO nanowires based UV photodiodes. Sensors Actuators A Phys. **127**, 201 (2006)
7. G. Li, J. Zhang, X. Hou, Temperature dependence of performance of ZnO-based metal-semiconductor-metal ultraviolet photodetectors. Sensors Actuators A Phys. **209**, 149 (2014)
8. Z. Zhang, W. Zhang, D. Zhang, Y. Xiao, J. Deng, G. Xia, Comparison of different characteristic parameters acquired by UV imager in detecting corona discharge. IEEE Trans. Dielectr. Electr. Insul. **23**, 1597 (2016)
9. T. Okino, S. Yamahira, S. Yamada, Y. Hirose, A. Odagawa, Y. Kato, T. Tanaka, Ultraviolet and visible spectral imaging of hydrogen flames using an organic photoconductive film CMOS imager, in *Proceedings of the International Image SensorWorkshop*, Hiroshima, vol. 30 (2017), pp. 188–191
10. T. Okino, S. Yamahira, S. Yamada, Y. Hirose, A. Odagawa, Y. Kato, T. Tanaka, A real-time ultraviolet radiation imaging system using an organic photoconductive image sensor. Sensors **18**, 314 (2018)
11. T.D. Moustakas, R. Paiella, Optoelectronic device physics and technology of nitride semiconductors from the UV to the terahertz. Rep. Prog. Phys. **80**, 106501 (2017)
12. S. Shinde, C. Bhosale, K. Rajpure, N-doped ZnO based fast response ultraviolet photoconductive detector. Solid State Electron. **68**, 22 (2012)
13. E. Munoz, E. Monroy, J. Pau, F. Calle, F. Omnes, P. Gibart, III nitrides and UV detection. J. Phys. Condens. Matter **13**, 7115 (2001)
14. Y. Duan, M. Cong, D. Jiang, Z. Guo, X. Zhou, N. Hu, K. Yu, ZnO ultraviolet photodetector-based metal-semiconductor-metal structure, *in Young Scientists Forum 2017*, vol. 10710 (International Society for Optics and Photonics, 2018), p. 107100X
15. H.-P. Lin, X.-J. Lin, D.-C. Perng, Electrodeposited CuSCN metal-semiconductor metal high performance deep-ultraviolet photodetector. Appl. Phys. Lett. **112**, 021107 (2018)
16. H. Ferhati, F. Djeffal, New high performance ultraviolet (MSM) TiO2/glass photodetector based on diffraction grating for optoelectronic applications. Optik Int. J. Light Electron Opt. **127**, 7202 (2016)
17. S. Mohammadnejad, S.E. Maklavani, E. Rahimi, Dark current reduction in ZnO based MSM photodetectors with interfacial thin oxide layer, in *International Symposium on High Capacity Optical Networks and Enabling Technologies, 2008 (HONET 2008)* (IEEE, 2008), pp. 259–264

18. X. Yang, D. Jiang, Z. Guo, W. Zhang, N. Hu, Y. Duan, S. Gao, Q. Liang, T. Zheng, J. Lv, Improving performance of the MgZnO ultraviolet photodetectors by changing the interdigital electrode width. Mater. Res. Bull. **98**, 275 (2018)
19. H.-Y. Chen, K.-W. Liu, X. Chen, Z.-Z. Zhang, M.-M. Fan, M.-M. Jiang, X.-H. Xie, H.-F. Zhao, D.-Z. Shen, Realization of a self-powered ZnO MSM UV photodetector with high responsivity using an asymmetric pair of au electrodes. J. Mater. Chem. C **2**, 9689 (2014)
20. J. Edmond, H. Kong, A. Suvorov, D. Waltz, C. Carter Jr., 6H-silicon carbide light emitting diodes and UV photodiodes. Phys. Status Solidi (a) **162**, 481 (1997)
21. X. Chen, H. Zhu, J. Cai, Z. Wu, High-performance 4H-SiC-based ultraviolet p-i-n photodetector. J. Appl. Phys. **102**, 024505 (2007)
22. S. Biondo, M. Lazar, L. Ottaviani, W. Vervisch, V. Le Borgne, M.A. El Khakani, J. Duchaine, F. Milesi, O. Palais, D. Planson, 4H-silicon carbide thin junction based ultraviolet photodetectors. Thin Solid Films **522**, 17 (2012)
23. H. Zhu, X. Chen, J. Cai, Z. Wu, 4H–SiC ultraviolet avalanche photodetectors with low breakdown voltage and high gain. Solid State Electron. **53**, 7 (2009)
24. X. Bai, X. Guo, D.C. Mcintosh, H.-D. Liu, J.C. Campbell, High detection sensitivity of ultraviolet 4H-SiC avalanche photodiodes. IEEE J. Quantum Electron. **43**, 1159 (2007)
25. H. Liu, D. Mcintosh, X. Bai, H. Pan, M. Liu, J.C. Campbell, H.Y. Cha, 4H-SiC pin recessed-window avalanche photodiode with high quantum efficiency. IEEE Photon. Technol. Lett. **20**, 1551 (2008)